Hindawi
Journal of Nanomaterials
Volume 2021, Article ID 4636531, 16 pages
https://doi.org/10.1155/2021/4636531

Research Article

Fabrication and Response Surface Methodology for the Adsorption of Nickel Ferrite-Graphene Oxide Nanocomposite for the Removal of Methylene Blue from Water

Lu Thi Mong Thy,[1,2,3] Nguyen Thi Chi Linh,[1] Nguyen Thi Tuyet Tram,[1] Tran Hoang Tu,[1] Le Tan Tai,[1,4] Pham Tan Khang,[1,4] Hoang Minh Nam,[2,4] Nguyen Huu Hieu ,[1,2,4] and Mai Thanh Phong [2,4]

[1]*VNU-HCM Key Laboratory of Chemical Engineering and Petroleum Processing (CEPP Lab), Vietnam*
[2]*Vietnam National University Ho Chi Minh City, Linh Trung Ward, Thu Duc District, Ho Chi Minh City, Vietnam*
[3]*Faculty of Chemical Engineering, Ho Chi Minh City University of Food Industry, 140 Le Trong Tan Street, Tay Thanh Ward, Tan Phu District, Ho Chi Minh City, Vietnam*
[4]*Faculty of Chemical Engineering, Ho Chi Minh City University of Technology (HCMUT), 268 Ly Thuong Kiet Street, Ward 14, District 10, Ho Chi Minh City, Vietnam*

Correspondence should be addressed to Nguyen Huu Hieu; nhhieubk@hcmut.edu.vn
and Mai Thanh Phong; mtphong@hcmut.edu.vn

Received 10 June 2020; Revised 23 November 2020; Accepted 25 December 2020; Published 15 January 2021

Academic Editor: Ester Vazquez

This study is aimed at studying the adsorption of methylene blue (MB) from aqueous solutions by nickel ferrite/graphene oxide (NGO) nanocomposite. The nanocomposite was characterized by Fourier transform infrared spectroscopy, X-ray diffraction, X-ray photoelectron spectroscopy, transmission electron microscopy, energy dispersive X-ray, Brunauer-Emmett-Teller-specific surface area, and vibrating sample magnetometer analyses. The interactive effects of critical variables including pH, initial concentration, and contact time on the adsorption capacity of NGO for MB were studied using response surface methodology (RSM) according to composite central design. In RSM models, the predicted values agreed well with verification experiments, with a high correlation coefficient of 0.9887. The adsorption process followed the pseudo-second-order kinetic and Langmuir isotherm models. The maximum capacity for adsorption of MB onto NGO was found to be 476.19 mg/g. Based on these results, NGO has the potential as an efficient adsorbent for the removal of MB from water.

1. Introduction

Recently, water pollution has been taken into account as an insurmountable problem by the rapid industrialization occurring in many parts of the world. The release of contaminants resulting from industrial activities into water reservoirs has negative impacts on people's health as well as afflicting harmful damage to living organisms [1]. In other words, many industrial fields like textile, printing, painting, pesticides, or even fertilizers are common pollutants of wastewater. This poses a serious threat to ecosystems, especially with aquatic creatures, as well as human well-being like carcinogenic agents [2]. The most chemical dye found from water is methylene blue (MB) as a phenothiazine dye. Consequently, the removal of MB plays an essential role in protecting natural habitat and the preservation of human health [3].

To deal with the poisonous reasons for MB, various attempts were made to eliminate them including ultrafiltration, sedimentation, coagulation-flocculation, and biological processes. However, these methods still exist limitations about the capacity to remove toxic organic compounds into nondangerous compounds due to their complex structure

Table 1: The variability of factors to MB adsorption capacity.

No.	Factors	Symbols	Values				
			$-\alpha$	-1	0	1	α
1	pH	A	7.32	8	9	10	10.68
2	Initial concentration (ppm)	B	231.82	300	400	500	568.18
3	Time (min)	C	2.50	40	95	150	187.50

With $\alpha = 1.68$.

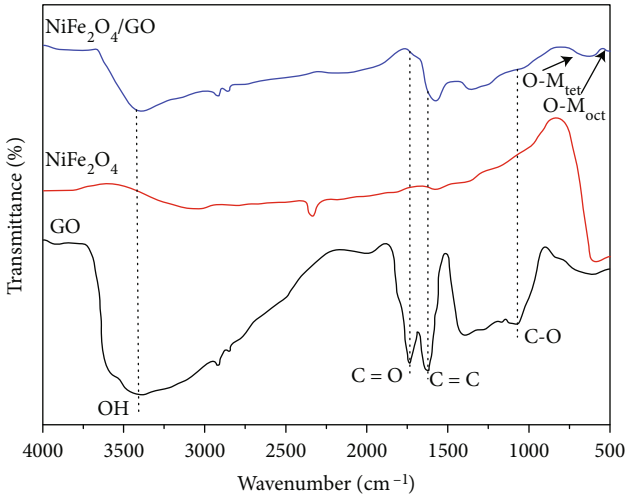

Figure 1: FTIR spectra of GO, $NiFe_2O_4$, and NGO.

[4, 5]. Besides, the adsorption method stands out as a durable process and an effective and promising way to solve aqueous solutions containing pollutants due to some advantages including economical concern, high flexibility, easy operation and manufacture, and high sensitivity to hazardous substances [6]. Therefore, the appearance of suitable and effective adsorbents for the development of adsorption of dyes from the aqueous environment has been paid attention around the world, especially with the application of nanoparticles as an adsorbent, possessing high efficiency of removal of contaminants in water [7].

Graphene oxide (GO) can be mentioned as another popular adsorbent with high surface area as well as containing oxygenated functionalities including hydroxyl (–OH), carbonyl (–C=O), carboxylic (–COOH), and epoxide (–O–) groups, which lead to the fact that GO has hydrophilicity and high negative charge density [8, 9]. Because GO is well dispersed in water, the ability to separate and recover the material is not high, which significantly limits its applications [10]. Thus, it is necessary to combine GO with another agent such as metal oxide to increase the selectivity and the recoverability of the adsorbent. The study of a literature survey of graphene-based composites such as Fe_3O_4/GO, Mn_3O_4/GO, and $MnFe_2O_4$/GO for the removal of pollutants from water has been prepared. Among the available oxides, nickel spinel ferrite ($NiFe_2O_4$) was chosen due to an inverse spinel structure with Ni^{2+} ions located at octahedral lattices which leads to the low saturated magnetization and high electrical resistivity of $NiFe_2O_4$. The nickel spinel ferrites (NF) is one of the soft ferrites, possessing a comparatively narrow bandgap which is attracting attention to scientists in the field of wastewater treatment as their exceptional magnetic response and chemical stabilities like magnetoconductivity and low hysteresis loss [11, 12]. This oxide is chosen as a promising base metal oxide nanocomposite due to characteristic properties of Ni^{2+} such as high catalytic efficiency with great ability of high transferring charge [10]. The nickel ferrite/graphene oxide (NGO) is proposed as an adsorbent for the removal of pollutants, especially for MB.

Besides, the optimization process which is built to improve the performance has received much attention from researchers [13]. To enhance the efficient removal of contaminants from aqueous solution and to boost adsorption productivity, it is necessary to investigate the optimization [14]. In this context, the response surface methodology (RSM) involving central composite design (CCD) is employed as the optimization study to investigate the effect of input parameters. In particular, the RSM involving mathematical and statistical procedures depended on the interaction of empirical models to the experimental data achieved from the construction of experiments, which has been considered as the most suitable technique applied to analytical optimization in processing multivariable [15]. An attractive advantage of this method is to reduce the number of experiments, so it can benefit the time and finance problem of the adsorption [14]. Among the RSM designs, CCD is one of the most popular methods due to its simplicity in structure and high achievement for efficiency. CCD brings several advantages including the decrease in the number of experiments and effective predictions in investigating the interaction factors [16]. Besides, CCD illustrates a 2-dimensional surface response graph and finds out the interaction of any two parameters and their effect on the response via polynomial equations [17]. Furthermore, two prominent approaches to study and conduct the optimization of the effect of input variables, including RSM with CCD, are also adopted.

In the present study, the NGO was synthesized by the coprecipitation method to adsorb MB from water. The structure and morphology of the nanocomposite were characterized by Fourier transform infrared spectroscopy (FTIR), X-ray diffraction (XRD), X-ray photoelectron spectroscopy (XPS), transmission electron microscopy (TEM), energy dispersive X-ray (EDX), Brunauer-Emmett-Teller-specific surface area (BET), and vibrating sample magnetometry (VSM). The interactive effects of critical variables on the adsorption capacity of NGO for MB were studied according to RSM. The experiment data were analyzed to study the kinetic and isotherm models and mechanisms. Besides, the regeneration experiments of material were also constructed.

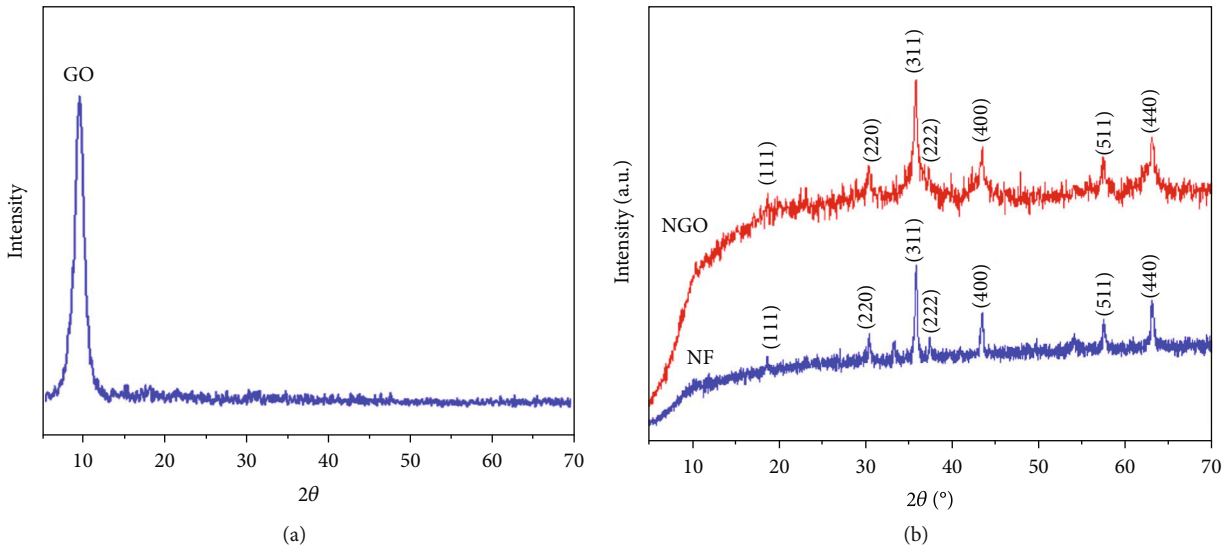

Figure 2: XRD patterns of (a) GO, (b) NF, and NGO.

2. Material and Methods

2.1. Material. Graphite powder (20 μm) was purchased from Sigma-Aldrich (Germany). All analytical grade chemicals, including H_2SO_4 (98 wt.%), H_3PO_4 (85 wt.%), HCl (36 wt.%), $FeCl_3.6H_2O$ (99 wt.%), $NiCl_2.4H_2O$ (99 wt.%), H_2O_2 (30 wt.%), and MB ($C_{16}H_{18}ClN_3S$, >99 wt.%), were purchased from Xilong Chemical (China). $KMnO_4$ (99 wt.%), NaOH (99 wt.%), and C_2H_5OH (99 wt.%) were obtained from Vina Chemsol (Vietnam).

2.2. Methods

2.2.1. Preparation of NGO. GO was fabricated by improved Hummer's method [18]; NF particles were synthesized by the coprecipitation method [19]. The NGO composite was synthesized by coprecipitation [20], with the weight of $NiFe_2O_4$ in NGO was 30%. Briefly, 0.5426 g $NiCl_2.6H_2O$ and 1.2349 g $FeCl_3.6H_2O$ were mixed in 250 mL GO suspension (5 g/L). Then, 2 M of NaOH solution was added drop by drop to the mixture until pH 12 was reached. The mixture was heated at 80°C under stirring for an hour before cooled to room temperature. The black precipitate was separated by an external magnetic field, washed with water, ethanol, and finally dried at 50°C.

2.2.2. Characterization. The functional groups on the surface of materials were studied with the FTIR spectrum (Tensor 27, Bruker). The crystal structure of the materials was analyzed via the D8 ADVANCE Bruker powder diffractometer with a Cu-K_α excitation source. The morphologies of the materials were identified by TEM (JEM 2100, Jeol, Japan) with a 200 kV accelerating voltage source. EDX spectra (Jeol-JMS 6490, Japan) was applied to determine the elemental compositions of materials. Valence states were analyzed using XPS (AXIS Supra, Kratos) with a monochromatized Al-K_α X-ray source (1486.6 eV). The specific surface areas of the material were measured through the BET method (Nova 3200e, Quantachrome). Lastly, the saturation magnetization value of the nanocomposite was recorded using VSM–7400 (MicroSense Easy VSM v. 9.13 L).

2.2.3. Experimental Design. The experiments were set up by adding 0.02 g of NGO into 20 mL MB solution. After the adsorption process, the MB concentration was determined by ultraviolet-visible spectroscopy (UV-Vis, Horiba Dual FL, Japan). The adsorption capacity (q, mg/g) of NGO was calculated according to equation (1).

$$q = \frac{(C_o - C_e)V}{m} \quad (1)$$

where C_o and C_e (ppm) are the initial and equilibrium concentrations of MB, respectively, V (mL) is the volume of MB solution, and m (mg) is the mass of the adsorbent [21].

RSM with CCD model was applied to investigate the simultaneous effects of factors on adsorption ability, including that of pH, initial MB concentration (ppm), and contact time (min). Table 1 shows the range of independent variables in the experimental design.

According to the CCD model, with the number of survey elements $k = 3$ and the number of experiments at the center $n_o = 6$, the total number of experiments (N) was calculated according to equation (2):

$$N = 2^k + 2k + n_o = 20. \quad (2)$$

The quadratic response surface model was fitted to the following equation (3):

$$Y = b_o + b_1X_1 + b_2X_2 + b_3X_3 + b_{11}X_1^2 + b_{22}X_2^2 + b_{33}X_3^2 + b_{12}X_1X_2 + b_{13}X_1X_3 + b_{23}X_2X_3, \quad (3)$$

where Y is the response (adsorption performance); X_1, X_2, and X_3 are the variables of the survey elements; b_o is a constant coefficient; b_1, b_2, and b_3 are the first-order coefficients; b_{11}, b_{22}, and b_{33} are the second-order coefficients; and b_{12},

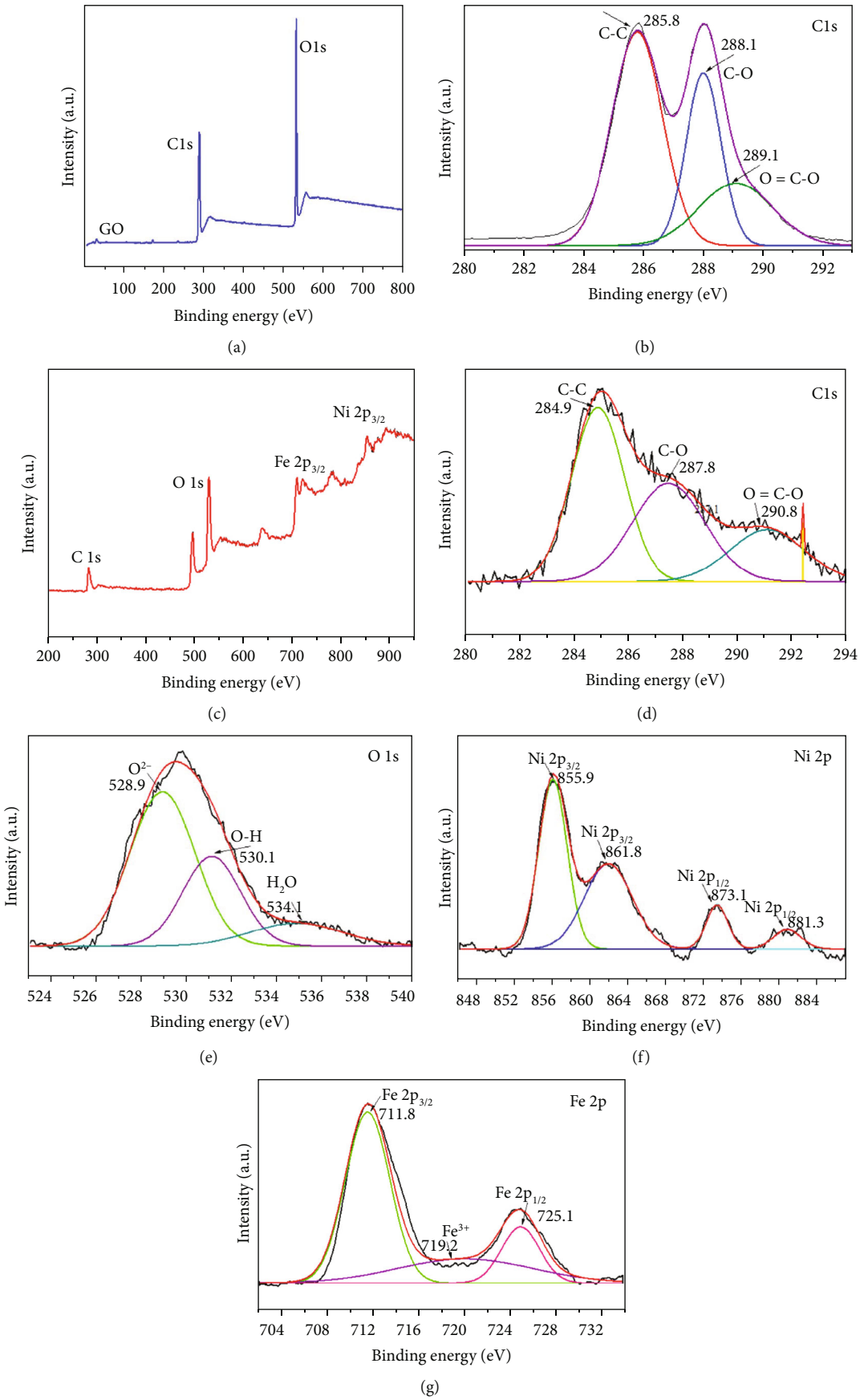

Figure 3: XPS spectra of (a) GO, (b) C 1s of GO, (c) NGO, (d) C 1s, (e) O 1s, (f) Ni 2p, and (g) Fe 2p of NGO.

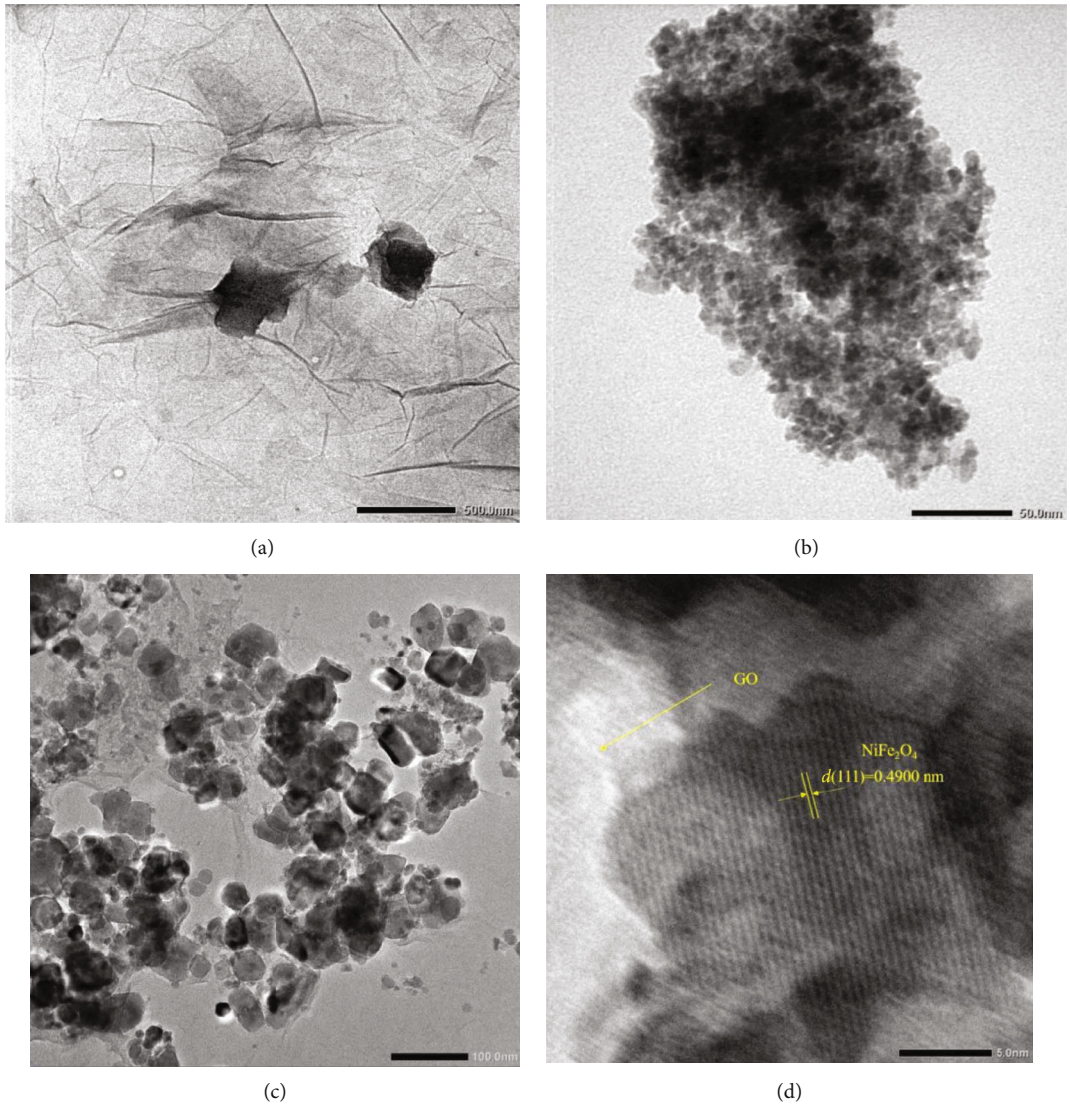

Figure 4: TEM images of (a) GO, (b) NF, (c), and (d) NGO.

Table 2: Weight percentage of each component in GO and NGO.

Materials	Mass (wt.%)			
	C	O	Fe	Ni
GO	50.09	49.91	—	—
NGO	49.59	28.03	14.63	7.75

b_{13}, and b_{23} are the interactive coefficients. The statistical parameters were assessed using an analysis of variances (ANOVA) via the Design Expert 10 software.

3. Results and Discussion

3.1. Characterization. The FTIR spectra were utilized to elaborate the functional groups on GO and NGO as shown in Figure 1. GO exhibited a strong absorption band at 3414.01 cm^{-1}, which corresponds to a characteristic band of –OH. The absorption band at about 1721.06 cm^{-1} is assigned to the C=O (carbonyl) groups, while the absorption bands at 1601.03, 1382.55, and 1041.02 cm^{-1} are C=C (aromatic), C–O (epoxide), and C–O (alkoxy), respectively. In the NGO and $NiFe_2O_4$ spectrum, the absorption bands were attributed to Ni–O (O–M_{tet}) and Fe–O (O–M_{oct}) linkages, which appeared at 624.33 and 434.78 cm^{-1}. The results indicated that $NiFe_2O_4$ nanoparticles have been linked on GO sheets [22].

The XRD patterns of GO, $NiFe_2O_4$, and NGO are displayed in Figure 2. The unique peak of the bare GO appeared at $2\theta = 9.47°$, indicating successful oxidation and exfoliation of GO [23]. The peaks of NGO appeared at $2\theta = 18.25$, 30.29, 35.68, 37.25, 43.30, 57.34, and 62.95, corresponding to those of $NiFe_2O_4$ including (111), (220), (311), (222), (400), (511), and (440) planes. The diffraction peak of GO did not exist as shown in Figure 2(b) due to the high diffraction intensities of $NiFe_2O_4$ particles overwhelming the weak GO peak. These results also indicate that the order of crystal structures in GO remained after the attachment with NF nanoparticles [24, 25].

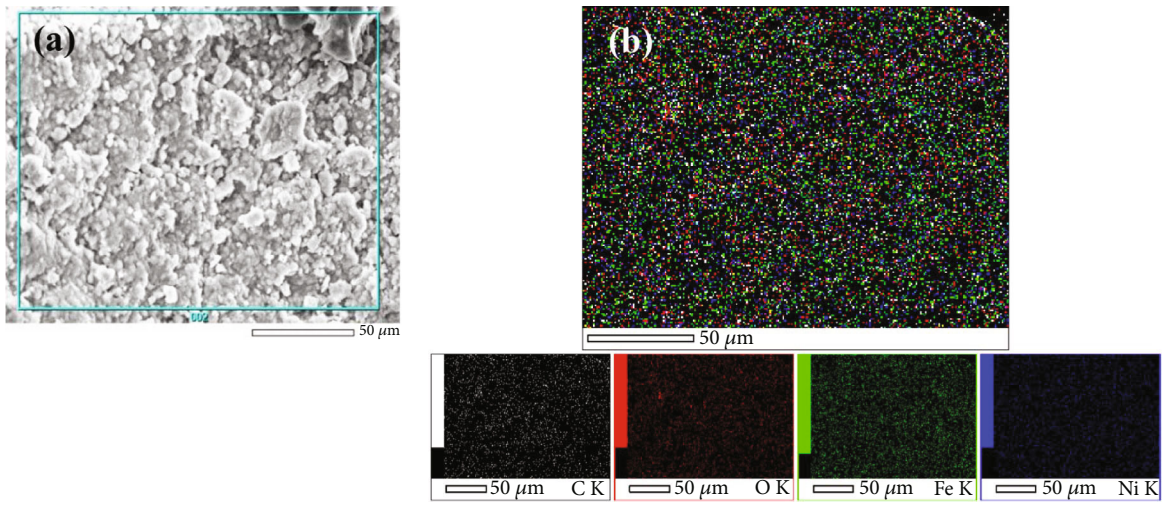

(a) (b)

Figure 5: (a) SEM image and (b) the distribution of elements of NGO.

Table 3: BET-specific surface areas of NGO and other materials.

Material	BET surface areas (m^2/g)	References
NGO	100.49	(This study)
GO	84.68	(This study)
$NiFe_2O_4$	63.70	[31]
$NiFe_2O_4$/GO	57.11	[31]

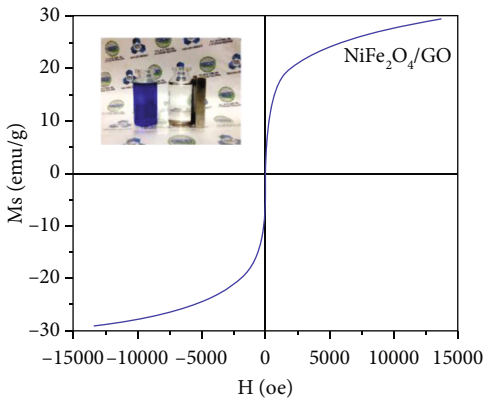

Figure 6: Magnetic curve of NGO.

Table 4: Saturated magnetism values of NGO.

Materials	Saturated magnetism (emu/g)	References
NGO	29.4	(This study)
$NiFe_2O_4$	39.6	[33]
$NiFe_2O_4$/GO	2.4	[31]
$CoFe_2O_4$/GO	4.5	[31]
$MnFe_2O_4$/GO	12.0	[34]

The XPS spectrum of GO and NGO is shown in Figure 3. As shown in C 1s, the spectrum of GO and NGO shows the presence of oxygen-functional groups associated with the carbon structures including C-C (285.8, 284.9 eV), C-O (288.1, 287.8 eV), and O=C-O (289.1, 290.8 eV), respectively. However, the signal strength of the C=O groups in the displacement NGO compared with GO was explained by the Ni^{2+} and Fe^{3+} ions linked with the oxygen-containing functional groups of GO. In the O1s spectrum (Figure 3(e)), the peaks at 528.9, 530.1, and 534.1 eV correspond to the presence of O^{2-}, O-H bond, and adsorbed H_2O, respectively. The presence of the O^{2-} bond in the NGO determines the Fe or Ni-O-C bond formation [26, 27]. The XPS spectrum

Table 5: Adsorption capacities of NGO for MB according to experimental design.

No.	A (pH)	B (ppm)	C (min)	Adsorption capacities (mg/g)
1	10	500	150	343.97
2	8	500	150	313.52
3	10	300	150	295.00
4	8	300	150	289.79
5	10	500	40	219.99
6	8	500	40	195.70
7	10	300	40	239.80
8	8	300	40	246.68
9	7.32	400	95	250.54
10	10.68	400	95	298.16
11	9	568.18	95	277.66
12	9	231.82	95	265.77
13	9	400	187.5	323.22
14	9	400	2.5	165.82
15	9	400	95	271.54
16	9	400	95	265.26
17	9	400	95	265.54
18	9	400	95	276.15
19	9	400	95	267.89
20	9	400	95	272.66

Table 6: Estimated coefficient of variables.

Factor	Estimated coefficient	Standard deviation
X_o	269.68	2.77
A	9.75	1.83
B	1.60	1.83
C	44.29	1.83
AB	7.05	2.40
AC	2.28	2.40
BC	17.94	2.40
A^2	2.63	1.79
B^2	1.70	1.79
C^2	-7.91	1.79

Table 7: ANOVA for adsorption of MB.

Factor	Sum of square	F-value	p value Prob > F	Reliability
X_o	32274.46	78.00	<0.0001	Reliable
A	1298.50	28.24	0.0003	Reliable
B	35.10	0.76	0.4028	Unreliable
C	26785.98	582.65	<0.0001	Reliable
AB	397.44	8.65	0.0148	Reliable
AC	41.62	0.91	0.3638	Unreliable
BC	2573.60	55.98	<0.0001	Reliable
A^2	99.74	2.17	0.1715	Reliable
B^2	41.65	0.91	0.3637	Unreliable
C^2	902.76	19.64	0.0013	Reliable
Residual	459.74			
Incompatibility	365.69	3.88	0.0812	Unreliable
Errors	94.04			
Total correlation	32734.19			

Table 8: Results of the suitability of the model and experimental data.

Parameters	Values	Parameters	Values
Standard deviation	6.78	R^2	0.9860
Mean value	267.23	R^2-correction	0.9733
Coefficient of variation CV%	2.54	R^2-prediction	0.9109

of Ni 2p (Figure 3(f)) is divided into two regions of Ni 2p3/2 (the peak of 855.9, 861.87 eV) and Ni 2p1/2 (the peak of approximately 873.1, 881.3 eV), indicating the presence of Ni^{2+} in the NGO. Two characteristic peaks in Figure 3(g) was centered at binding energies of 711.8 and 725.1 eV due to Fe 2p3/2 and Fe 2p1/2, respectively. In addition, another peak at 719.2 eV also created the presence of Fe^{3+} in the XPS analysis of $NiFe_2O_4$ following XRD and FTIR [28, 29].

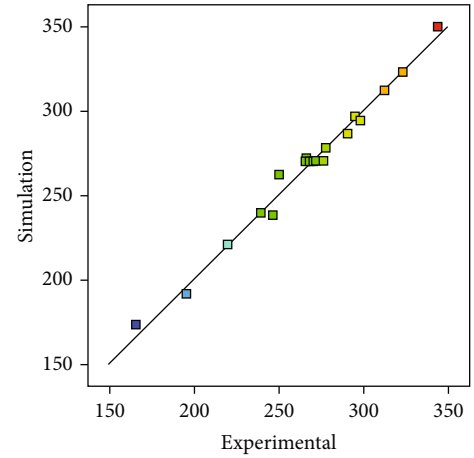

Figure 7: MB adsorption capacity from experimental and simulated data.

Table 9: Analytical and experimental adsorption capacity.

pH	Time (min)	MB initial concentration (ppm)	Adsorption capacity (mg/g) Simulation	Experiment
10	150	500	329.95	343.65

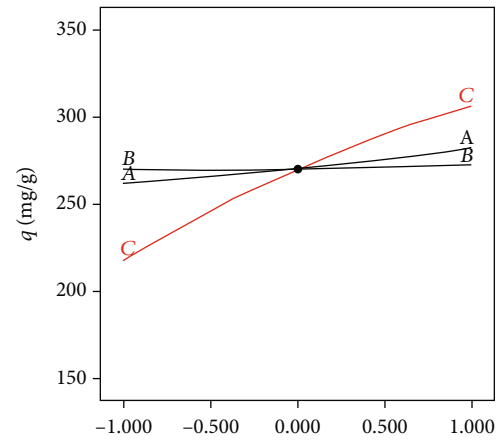

Figure 8: The impact of each factor on NGO adsorption capacity for MB.

The TEM images of GO, $NiFe_2O_4$, and NGO are shown in Figure 4. GO sheets were flat, which showed the highly oxidized and exfoliated attributes of GO; however, the wrinkles and folds of GO appeared, which showed the stacking of sheets. For $NiFe_2O_4$, the image was presented with many overlapped black dots forming several black portions, indicating the agglomeration of particles. For NGO, the $NiFe_2O_4$ nanoparticles were distributed uniformly on the GO surface, with an average size of 5-10 nm. These results can be explained by the effect of electrostatic interactions between GO and NF, which helped to prevent the agglomeration and stabilization of $NiFe_2O_4$ nanoparticles [30]. On a smaller scale, as shown in Figure 4(d), the HR-TEM image also showed the

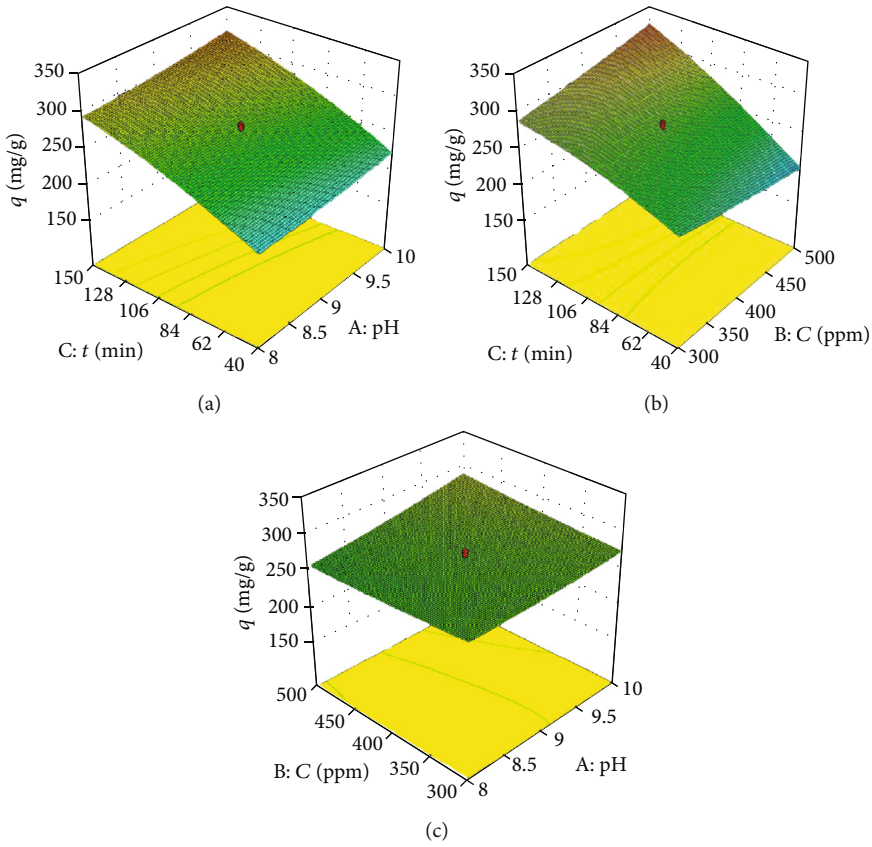

Figure 9: The effect of each pair of factors on the adsorption capacity (a) pH and time; (b) time and initial concentration; and (c) pH and initial concentration.

presence of one peak (111) with an interplanar spacing of 0.49 nm corresponding to a crystal plane of $NiFe_2O_4$ found on the GO sheets. This result is a good agreement with the results of XRD analysts. As a result, the comparison of the TEM and HR-TEM images between the bare GO and NGO revealed that $NiFe_2O_4$ nanoparticles were successfully decorated on the GO surface [28].

The element compositions of GO and NGO were determined through EDX data (Table 2). The element compositions of Ni and Fe were confirmed with Ni and Fe wt.% of 7.75 and 14.63%, respectively, which was consistent with the nominal loading molar ratio of Ni/Fe in the starting salt solution. Figure 5 illustrates the SEM image and the distribution of elements in NGO. The Fe and Ni were uniformly dispersed on the C and O base, presenting the attachment of $NiFe_2O_4$ on the GO surface as well the effective decline of agglomeration on the material.

The BET surface area of the NGO was 100.49 m^2/g, while GO was 84.68 m^2/g. The formation of NF nanoparticles on the GO substrate expanded the interlayer spacing between GO sheets, increasing the surface area of the nanocomposite [22]. This result was higher than that of other magnetic nanocomposite materials as shown in Table 3.

As shown in Figure 6, the magnetic properties of the fabricated NGO indicate that it can be removed after the adsorption process and recycled by applying an external magnetic field. The saturation magnetization value (M_s) was 29.4 emu/g, which is lower than that of NF in Table 4. The decrease in the M_s value can be attributed to the smaller size of particles and the presence of nonmagnetic GO. The electron transfer from the nickel ferrite to GO reduces the magnetic moment, leading to the difference in the magnetic property of composite [32].

3.2. Influence of Factors on Adsorption Ability. RSM with CCD was employed to study the significance of the independent variables. In detail, pH (A), initial concentration (B), and contact time (C) were taken as input variables, and the adsorption capacity (Y) was taken as the response. Table 5 displays the experimental result of 20 runs, along with the experimental and predicted adsorption results for MB.

Based on the regression analysis, the estimated coefficients of the equation are shown in Table 6.

To analyze the relevance and significance of the model, it was assessed through ANOVA as shown in Table 7.

The regression coefficients were tested by the Fisher standard, with $p < 0.05$, suggesting that the regression coefficients are significant and that the model is a completely statistical analysis, with its reliability 99.99% ($p < 0.0001$). Moreover, the value of $F = 3.88$ and $p = 0.0812 > 0.05$ shows that the model is compatible with experiments. The adsorption capacity is correlated to the

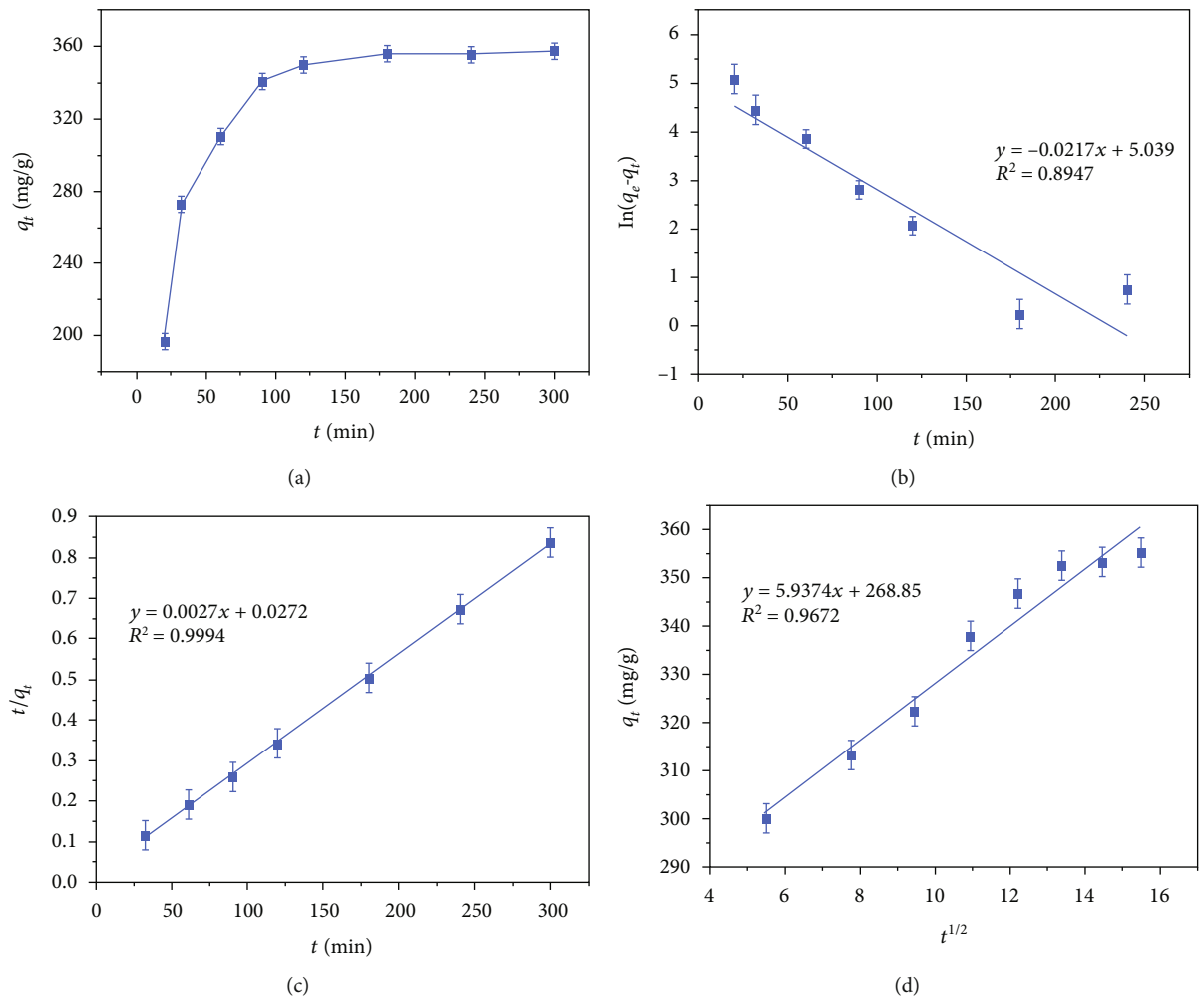

Figure 10: Effects of (a) time, (b) the linear plot of the pseudo-first-order, (c) pseudo-second-order, and (d) interparticle diffusion kinetic model on adsorption capacity of NGO for MB (mass adsorbent of 0.02 g, concentration of MB of 400 ppm, pH of 9).

Table 10: The parameters of kinetic models of NGO for MB adsorption.

Pseudo-first-order		Pseudo-second-order		Intreparticle diffusion	
k_1 (min^{-1})	R^2	k_2 (g/mg.min)	R^2	K_{id} ($\text{g/mg.min}^{0.5}$)	R^2
0.0352	0.9836	0.00028	0.9994	0.0027	0.9672

independent variables using the following second-order polynomial model that takes into account the individual, interactive, and quadratic terms as follows:

$$Y = 728.8133 - 69.7368A - 1.0641B - 0.3753C + 0.0705\text{AB} + 0.0415\text{AC} + 0.0033\text{BC} + 2.631A^2 + 0.00017B^2 - 0.0026C^2. \quad (4)$$

The appropriateness of the model with experiments was also based on the analytical values shown in Table 8. It shows the relevant and meaningful analysis of the model compared to the experiment. ANOVA analysis results show that the value of $R^2 = 0.9860$, which is close to 1; the coefficient of variation CV% = 2.54 and correction factor $R^2 = 0.9733$ show that the MB adsorption capacity of the NGO material is close to the model's predicted value.

The MB adsorption capacity of NGO in experiments and simulations is shown in Figure 7. The experimental values compared with simulated data have high correlation coefficients, which confirms their compatibility. The regression model is shown to be suitable to predict MB adsorption, with defined conditions related to the effect of pH value, adsorption time, and initial concentration of MB.

In applying the CCD model, the analytical adsorption capacity is compared with experimental results. This is shown in Table 9. Based on the model, the appropriate adsorption capacity is predicted to be 329.95 mg/g at pH 10, with an adsorption time of 150 minutes and an initial concentration

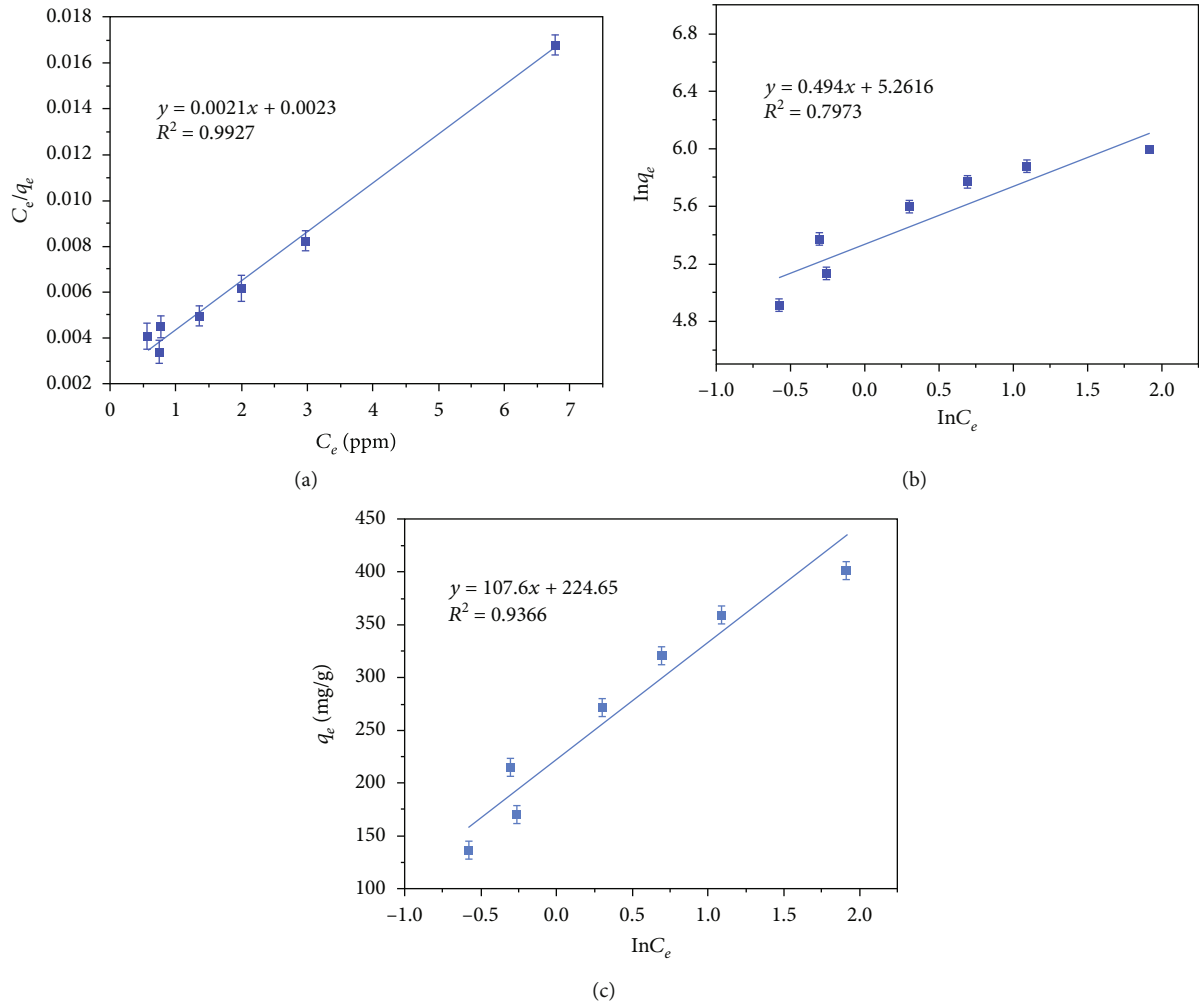

Figure 11: The (a) Langmuir, (b) Freundlich, and (c) Temkin model of NGO for MB adsorption (mass adsorbent of 0.02 g, time of 150 minutes, pH of 9).

Table 11: Langmuir and Freundlich adsorption models of NGO for MB.

Langmuir			Freundlich			Temkin		
k_l (l/mg)	q_{max} (mg/g)	R^2	n	k_f (mg/g)(l/mg)$^{1/n}$	R^2	B	k_T	R^2
0.913	476.19	0.9927	2.0243	192.789	0.7963	107.60	8.067	0.9365

of MB of 500 ppm. Based on the experiments, the adsorption capacity is 343.65 mg/g (less than 5% greater compared to the predicted results). This proves that the adsorption capacity of NGO for MB is congruent with the predictive model. Figure 8 shows the steepest curve C corresponding to the MB adsorption time; thus, the MB adsorption capacity of NGO is most prominently affected by adsorption time.

Three-dimensional curves were plotted to clarify the effects of process variables, with two factors for each graph shown in Figure 9. Figure 9(a) shows that the MB adsorption capacity of the material increases as pH and adsorption time increase. This shows that the higher the pH, the better the adsorbent material's performance. Similar to Figure 9(b), the longer the adsorption time, the better the contact between the material and the MB solution, and the higher the MB adsorption capacity of the material. Results showed that during the first 60 minutes, the adsorption process took place quickly, and the amount of MB absorbed from the solution was higher. After 150 minutes, the adsorption capacity increased more slowly. In this case, the amount of NGO absorbed by MB is almost unchanged. For Figure 9(c), which indicates the relationship between pH and concentration, at concentrations greater than 400 ppm and pH greater than 9, the adsorption capacity of the material nearly reaches equilibrium, and the adsorption rate slows down greatly.

3.3. Adsorption Kinetic. As time increased, the adsorption capacity of NGO for MB was enhanced as shown in

Table 12: Maximum MB adsorption capacities of NGO and other materials.

Materials	Maximum adsorption capacities (mg/g)	References
NGO	476.19	(This study)
$NiFe_2O_4$	40.13	(This study)
GO	165.68	(This study)
$NiFe_2O_4$/GO	78.10	[31]
Fe_3O_4/GO	64.23	[37]
$CoFe_2O_4$/GO	80.60	[31]
$MnFe_2O_4$/GO	177.30	[34]

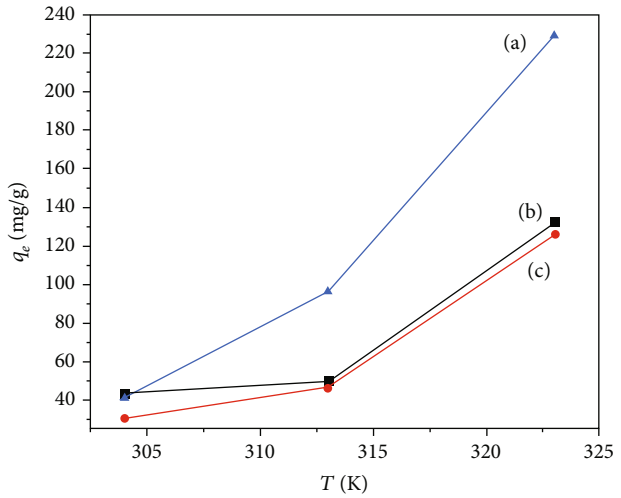

Figure 12: Effects of temperature on adsorption capacity of NGO for MB at the initial concentration (a) 34.30, (b) 65.08, and (c) 176.49 g/mL (mass adsorbent of 0.02 g, time of 150 min, pH of 9).

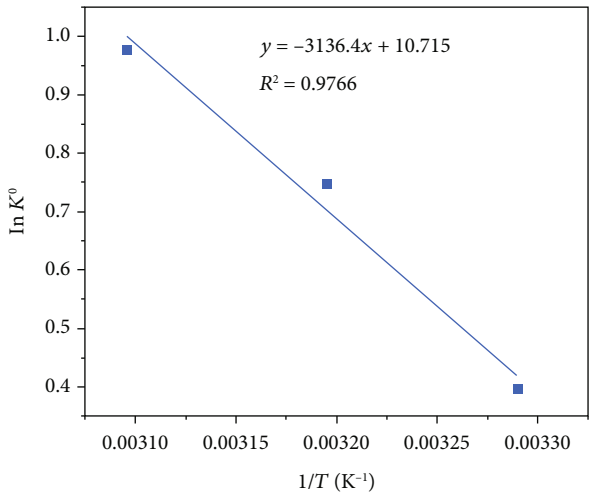

Figure 13: Variation of thermodynamic adsorption constant K° with $1/T$ of NGO for MB with initial concentrations 34.30, 65.08, and 176.49 g/mL.

Table 13: Thermodynamic parameters for MB adsorption of NGO.

Temperature (K)	K^o	ΔG (kJ/mol)	ΔH (kJ/mol)	ΔS (kJ/mol)
304	1.448	-0.5129		
313	2.115	-1.8057	23.589	0.0890
323	2.660	-2.0017		

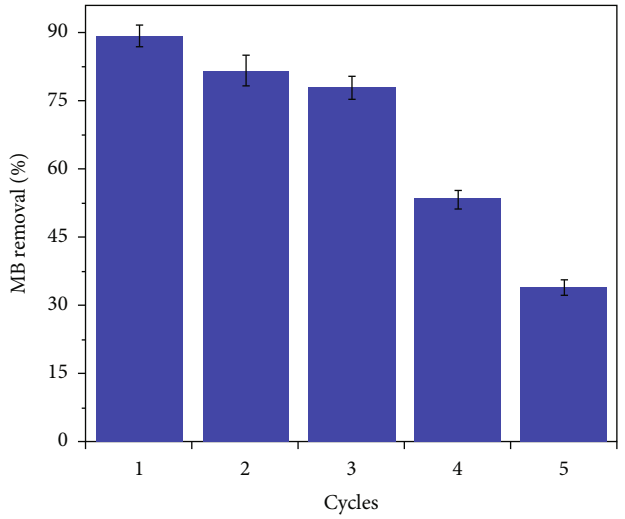

Figure 14: Recyclability experiment of NGO for MB adsorption.

Figure 10(a). The values of constants for the kinetic models were calculated and summarized in Table 10. Higher values of correlation coefficient (R^2) show the fitness of the sorption data; it may be inferred that the *pseudo-second-order* model has higher R^2 compared to *pseudo-first-order*, and the inter-particle diffusion kinetic models (Figure 10). In addition, based on the higher R^2 of the intraparticle diffusion, it is inferred that intraparticle diffusion plays a significant role in the adsorption of NGO for MB. The intraparticle diffusion process consisted of the following 3 steps: (1) film diffusion (from 0 to 60 minutes), (2) intraparticle or pore diffusion (from 60 to 150 minutes), and (3) sorption into interior sites (from 150 to 300 minutes). After 150 minutes, the active centers on the surface of the NGO were filled. The concentration of MB in the solution decreased, reducing the diffusion rate of MB into the material structure, so the adsorption capacity was little changed. Therefore, the appropriate MB adsorption time of the NGO is determined to be 150 [35].

3.4. Adsorption Isotherm. The Langmuir, Freundlich, and Temkin isotherm models were used to investigate the MB removal process of NGO [36]. Figure 11 and Table 11 present the linear plots and parameters of these models for MB adsorption.

Based on the experimental results, the adsorption process followed the Langmuir model with a correlation coefficient of nearly 1 ($R^2 = 0.9927$). Therefore, the operation resembles that of a single-layer adsorbent with a uniform adsorption surface, and the maximum MB adsorption capacity was $q_{max} = 476.19$ mg/g.

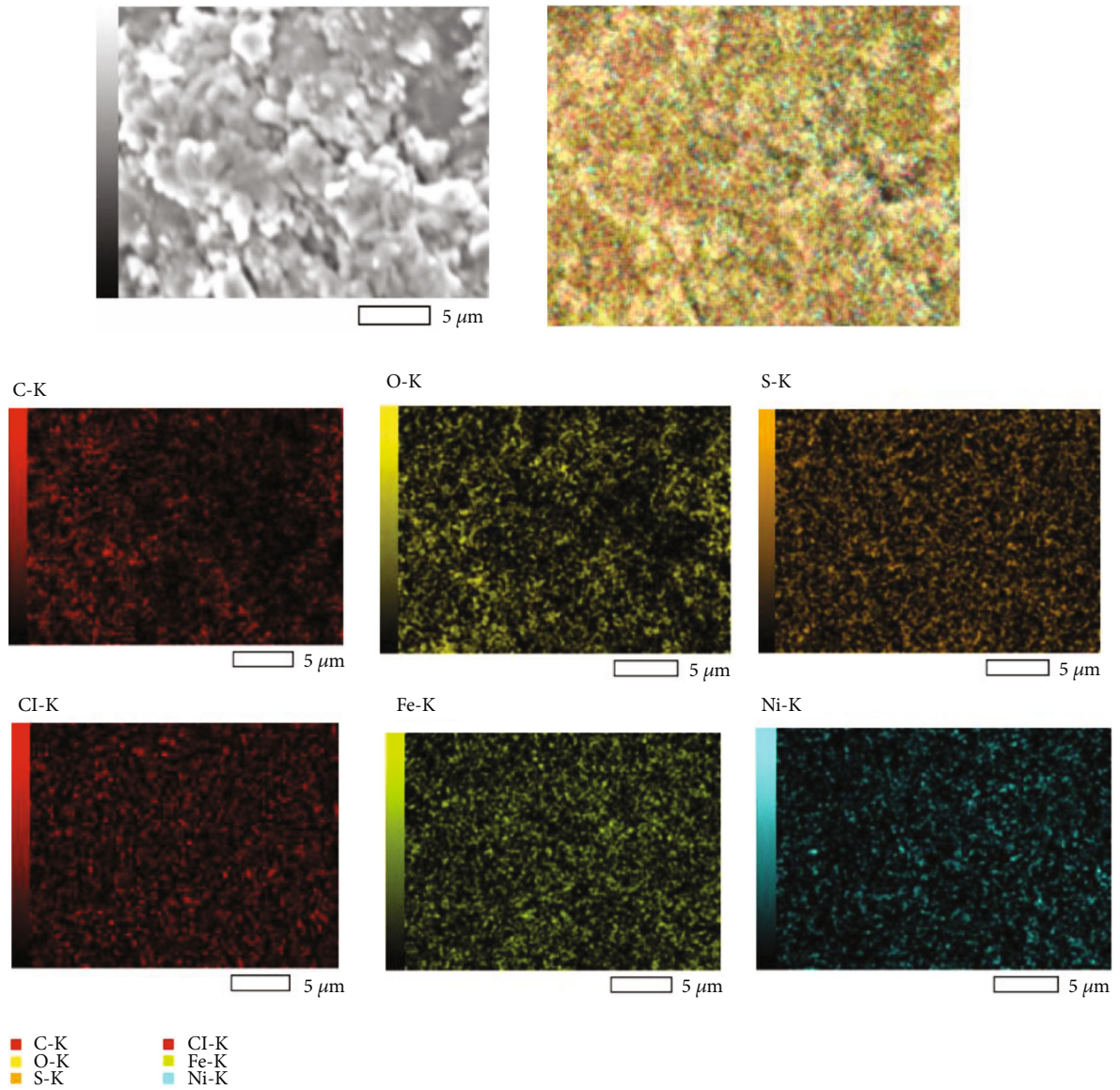

Figure 15: SEM image and elemental mapping in NGO after MB adsorption.

Table 14: The elemental compositions in NGO before and after MB adsorption.

Element	NGO	NGO_MB
C	49.59	35.06
O	28.03	33.76
Fe	14.63	18.10
Ni	7.75	10.39
S	—	2.61
Cl	—	0.08

The MB adsorption capacity of NGO is much higher than that of other adsorbent materials shown in Table 12. This result could be explained as follows: the attachment of $NiFe_2O_4$ nanoparticles on the GO surface increased the number of adsorption sites to link with MB. Besides, the process of transferring charged electrons from $NiFe_2O_4$ to the GO

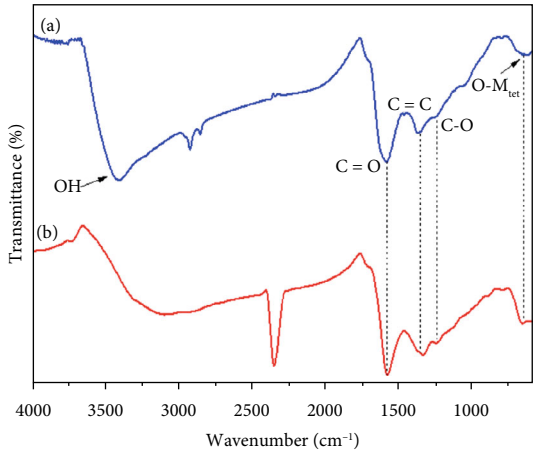

Figure 16: FTIR spectra of NGO (a) before and (b) after MB adsorption.

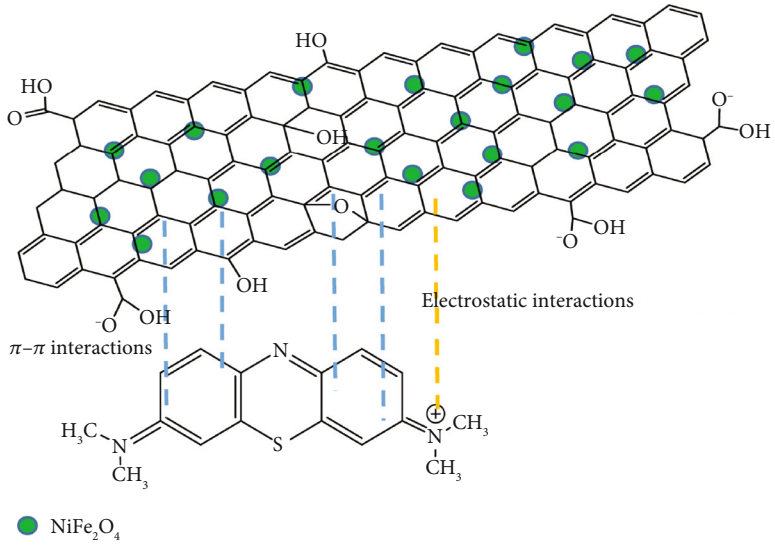

Figure 17: The adsorption mechanism of NGO for MB.

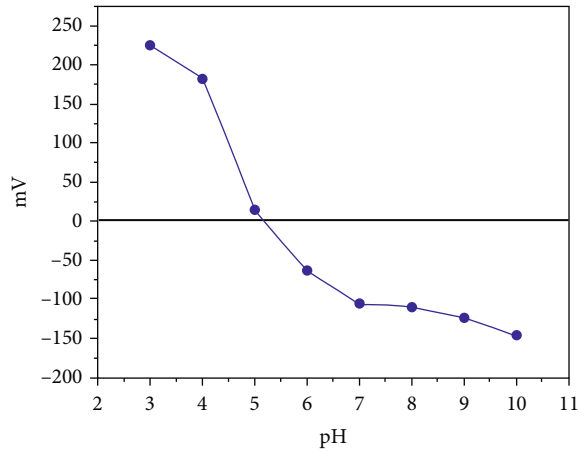

Figure 18: Zeta potential of NGO.

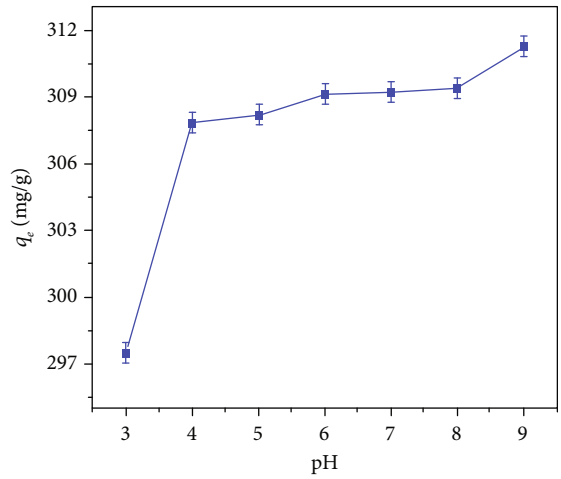

Figure 19: Effects of pH on adsorption capacity of NGO for MB (mass adsorbent of 0.02 g, concentration of MB of 400 ppm, time of 150 minutes).

surface increases interaction with MB, improving the processing efficiency [22].

3.5. Adsorption Thermodynamics. The investigation of the effect of temperature on the adsorption process was conducted at three different temperatures of 304, 313, and 323 K with the initial concentration of MB of 34.30, 65.08, and 176.49 g/mL. According to the results as shown in Figure 12, the increase in adsorption capacity following the increase in temperature results from the rise in diffusion and drop in viscosity of the adsorbent.

The thermodynamic functions including adsorption free energy change (ΔG°), standard enthalpy (ΔH°), and entropy (ΔS°) are evaluated based on the Van't Hoff equation:

$$\mathrm{Ln}K^{o} = \frac{-\Delta G^{o}}{\mathrm{RT}} = \frac{\Delta S^{o}}{\mathrm{R}} - \frac{\Delta H^{o}}{\mathrm{RT}} = \mathrm{Ln}\frac{q_e}{C_e}, \quad (5)$$

where K^o is the thermodynamic equilibrium constant, R is the universal gas constant (8.3145 J/mol·K), and T is the temperature of the solution (K). q_s is the amount of the MB adsorbed per unit gram of the adsorbent (mmol/g), and C_e is the equilibrium concentration of MB (mmol/mL).

The curve fitting and calculation results are listed in Figure 13 and Table 13. The negative value of ΔG° confirms that the adsorption process is spontaneous ($\Delta G^\circ < 0$). When the above relations are used, the value of ΔH° is positive in each case, confirming that the reaction is endothermic [38].

3.6. Reusability. After the MB adsorption process, NGO was regenerated by using various solvents namely ethanol, acetone, H_2O, HCl 0.01 M. The results showed that the efficiency

Table 15: Relationship between thermodynamic parameters and adsorption force [42].

Thermodynamic parameters	Adsorption force
$\Delta H > 0$, $\Delta S > 0$, $\Delta H < T\Delta S$	Hydrophobic interactions
$\Delta H < 0$, $\Delta S < 0$, $\Delta H \mid > \mid T\Delta S\mid$	Hydrogen bond and Van der Waals interactions
$\Delta H \sim 0$ or $\Delta H > 0$, $\Delta S > 0$	Electrostatic attraction

of the desorption by ethanol was higher than that of other desorption solutions. Figure 14 shows the results from five cycles of experiments conducted in the batch mode and the ability to reuse adsorption of material via 5 cycles decreased from 89.27 to 38.86%.

3.7. Adsorption Mechanism. The significant change of adsorbent after the adsorption process was investigated by using SEM-EDX and FTIR analysis. The SEM image shows that the MB changed the morphology of the adsorbent; the surface of the adsorbent is rough, and the edges became fuzzy after adsorption as shown in Figure 15. The elemental compositions of NGO before and after adsorption are shown in Table 14. The increase of C and O contents in nanocomposite was compared to NGO. And, the attendance of the S and Cl element displays that the MB molecules were adsorbed on the NGO surface. These results indicate that the adsorption is a series of interactions produced by functional groups of NGO and MB.

Figure 16 shows the FTIR spectra of NGO before and after MB adsorption. The decrease in the intensity of –OH, –C=O, C=C, and –C-O peaks was reported; thus, the acidic protons of oxygen-containing groups existed on the NGO surface were interacted with MB. The removal behavior of NGO for MB could be explained through hydrophobic and electrostatic interactions as shown in Figure 17. The hydrophobic planes of the NGO interact with the aromatic rings of the dyes, leading to strong $\pi - \pi$ stacking interactions under neutral conditions. The electrostatic attraction between the positively charged MB-N^+ and negatively charged NGO also provides a driving force for the adsorption [20]. These interactions between the dye molecules and adsorbent are responsible for the superior adsorption of the NGO nanocomposite [39, 40].

To evaluate the main adsorption mechanism of MB, the role of surface charge of adsorbent and adsorbate was discussed. Figure 18 shows the zeta potential of NGO, where the isoelectric point is at 5.14. The surface charge of NGO exists in cation at pH below 5.14 with the –OH and –COOH groups become positively charged $-OH_2^+$ and $-COOH_2^+$ groups. When pH is higher than 5.2, –OH and –COOH groups are ionized and NGO is negatively charged. Moreover MB is positively charged to MB^+ forms in a wide pH and is a cation dye. To influence the pH on the adsorption capacity, the experiments were prepared in the range of pH from 3 to 9 as shown in Figure 19. Hence, the adsorption ability of NGO is slightly increased when pH increase; there is a fraction of electrostatic interaction between NGO and MB. However, in general, the removal ability of NGO has no great changes under almost pH conditions; thus, the hydrophobic interactions play a key force in the adsorption process [38].

Besides, the above explanation agrees well with the thermodynamic calculation results. The value of $|\Delta G|$ is generally between 20 kJ/mol and 0 kJ/mol; thus, the adsorption process of MB on NGO suggests physisorption [41]. The adsorption mechanism was contributed by hydrophobic interaction, electrostatic interaction, hydrogen bond, or Van der Waals interaction [42]. Based on the values of ΔH and ΔS, the domain interaction was identified in the adsorption process as shown in Table 15. The adsorption process had entropically favorable ($\Delta S > 0$) and enthalpically unfavorable ($\Delta H > 0$), implying that the hydrophobic interaction was predominated.

4. Conclusions

$NiFe_2O_4$/GO nanocomposite was successfully synthesized by the coprecipitation method. The results of the characteristic analysis of NGO showed that NF nanoparticles were formed and linked on the surface of GO layers with sizes ranging from *10* to *20* nm. The saturation magnetism of NGO was 29.4 emu/g, and the specific surface area was 100.49 m^2/g. The simultaneous effects of the above adsorption conditions on the adsorption capacity of NGO for MB were investigated by experimental design according to RSM with the CCD model. The adsorption capacity reached 343.98 mg/g at conditions pH 10, 150 minutes, and MB initial concentration of 500 ppm. The adsorption process followed the pseudo-second-order kinetics and Langmuir adsorption principle, which is hypothesized to be monolayer adsorption. Based on these results, $NiFe_2O_4$/GO nanocomposite has potential applications in the field of MB adsorption.

Data Availability

The data that support the findings of this study are available from the corresponding author upon reasonable request.

Conflicts of Interest

The authors declare that there is no conflict of interest.

Acknowledgments

This research is funded by Ho Chi Minh City University of Technology, VNU-HCM, under grant number BK-SDH-2020-1880319.

References

[1] P. Annie Vinosha, B. Xavier, A. Ashwini, L. Ansel Mely, and S. Jerome Das, "Tailoring the photo-Fenton activity of nickel

ferrite nanoparticles synthesized by low-temperature coprecipitation technique," *Optik*, vol. 137, pp. 244–253, 2017.

[2] J. T. Adeleke, T. Theivasanthi, M. Thiruppathi, M. Swaminathan, T. Akomolafe, and A. B. Alabi, "Photocatalytic degradation of methylene blue by ZnO/$NiFe_2O_4$ nanoparticles," *Applied Surface Science*, vol. 455, pp. 195–200, 2018.

[3] G. M. B, M. J B, R. P, and H. K. M, "Equilibrium and kinetic studies on methylene blue adsorption by simple polyol assisted wet hydroxyl route of NiFe2O4nanoparticles," *Journal of Environmental Health Science and Engineering*, vol. 17, no. 2, pp. 539–547, 2019.

[4] R. D. Suryavanshi, S. V. Mohite, A. A. Bagade, S. K. Shaikh, J. B. Thorat, and K. Y. Rajpure, "Nanocrystalline immobilised ZnO photocatalyst for degradation of benzoic acid and methyl blue dye," *Materials Research Bulletin*, vol. 101, pp. 324–333, 2018.

[5] X. Chen, P. Wang, J. Xu et al., "Magnetic separation and adsorptive performance for methylene blue of mesoporous $NiFe_2O_4$/SBA-15 nanocomposites," *Advanced Powder Technology*, vol. 28, no. 9, pp. 2087–2093, 2017.

[6] M. Bayat, V. Javanbakht, and J. Esmaili, "Synthesis of zeolite/-nickel ferrite/sodium alginate bionanocomposite via a co-precipitation technique for efficient removal of water-soluble methylene blue dye," *International Journal of Biological Macromolecules*, vol. 116, pp. 607–619, 2018.

[7] N. H. Othman, N. H. Alias, M. Z. Shahruddin, N. F. Abu Bakar, N. R. Nik Him, and W. J. Lau, "Adsorption kinetics of methylene blue dyes onto magnetic graphene oxide," *Journal of Environmental Chemical Engineering*, vol. 6, no. 2, pp. 2803–2811, 2018.

[8] W. Peng, H. Li, Y. Liu, and S. Song, "A review on heavy metal ions adsorption from water by graphene oxide and its composites," *Journal of Molecular Liquids*, vol. 230, pp. 496–504, 2017.

[9] A. Molla, Y. Li, B. Mandal, S. G. Kang, S. H. Hur, and J. S. Chung, "Selective adsorption of organic dyes on graphene oxide: theoretical and experimental analysis," *Applied Surface Science*, vol. 464, pp. 170–177, 2019.

[10] L. P. Lingamdinne, J. R. Kodurua, Y. Y. Changa, and R. R. Karri, "Process optimization and adsorption modeling of Pb(II) on nickel ferrite-reduced graphene oxide nano-composite," *Journal of Molecular Liquids*, vol. 250, pp. 202–211, 2018.

[11] G. Zhao, L. Liu, J. Li, and Q. Liu, "Efficient removal of dye MB: through the combined action of adsorption and photodegradation from $NiFe_2O_4$/Ag_3PO_4," *Journal of Alloys and Compounds*, vol. 664, pp. 169–174, 2016.

[12] Y. Liang, Y. He, Y. Zhang, and Q. Q. zhu, "adsorption property of alizarin red S by $NiFe_2O_4$/polyaniline magnetic composite," *Journal of Environmental Chemical*, vol. 6, no. 1, pp. 416–425, 2018.

[13] A. Parnianifard, A. S. Azfanizam, M. K. A. Ariffin, and M. I. S. Ismail, "An overview on robust design hybrid metamodeling: advanced methodology in process optimization under uncertainty," *International Journal of Industrial Engineering Computations*, vol. 9, pp. 1–32, 2018.

[14] M. Wakkel, B. Khiari, and F. Zagrouba, "Basic red 2 and methyl violet adsorption by date pits: adsorbent characterization, optimization by RSM and CCD, equilibrium and kinetic studies," *Environmental Science and Pollution Research*, vol. 26, no. 19, pp. 18942–18960, 2019.

[15] T. van Thuan, B. T. P. Quynh, T. D. Nguyen, V. T. T. Ho, and L. G. Bach, "Response surface methodology approach for optimization of Cu^{2+}, Ni^{2+} and Pb^{2+} adsorption using KOH-activated carbon from banana peel," *Surfaces and Interfaces*, vol. 6, pp. 209–217, 2017.

[16] M. Dastkhoon, M. Ghaedi, A. Asfaram, A. Goudarzi, S. M. Mohammadi, and S. Wang, "Improved adsorption performance of nanostructured composite by ultrasonic wave: optimization through response surface methodology, Isotherm and kinetic studies," *Ultrasonics Sonochemistry*, vol. 37, pp. 94–105, 2017.

[17] B. Priya, S. Kaith, U. Shanker, B. Gupta, and J. K. Bhatia, "RSM-CCD optimized In-air synthesis of photocatalytic nanocomposite: application in removal-degradation of toxic brilliant blue," *Reactive and Functional Polymers*, vol. 131, pp. 107–122, 2018.

[18] J. Chen, B. Yao, C. Li, and G. Shi, "An improved Hummers method for eco-friendly synthesis of graphene oxide," *Carbon*, vol. 64, pp. 225–229, 2013.

[19] L. P. Lingamdinne, Y. L. Choi, I. S. Kim, Y. Y. Chang, J. R. Koduru, and J. K. Yang, "Porous graphene oxide based inverse spinel nickel ferrite nanocomposites for the enhanced adsorption removal of arsenic," *RSC advances*, vol. 6, no. 77, pp. 73776–73789, 2016.

[20] L. Thi Mong Thy, N. Hoan Kiem, T. Hoang Tu et al., "Fabrication of manganese ferrite/graphene oxide nanocomposites for removal of nickel ions, methylene blue from water," *Chemical Physics*, vol. 533, article 110700, 2020.

[21] R. Malik, S. Lata, and S. Singhal, "Evaluation of kinetics and adsorption isotherms for the elimination of Pb (II) from aqueous solutions using Aloe barbadensis Miller leaf powder," *Pollution*, vol. 1, no. 4, pp. 403–415, 2015.

[22] L. Kuang, Y. Liu, D. Fu, and Y. Zhao, "FeOOH-graphene oxide nanocomposites for fluoride removal from water: acetate mediated nano FeOOH growth and adsorption mechanism," *Journal of colloid and interface science*, vol. 490, pp. 259–269, 2017.

[23] D. C. Marcano, D. V. Kosynkin, J. M. Berlin et al., "Improved synthesis of graphene oxide," *ACS nano*, vol. 4, no. 8, pp. 4806–4814, 2010.

[24] V. Chandra, J. Park, Y. Chun, J. W. Lee, I. C. Hwang, and K. S. Kim, "Water-dispersible magnetite-reduced graphene oxide composites for arsenic removal," *ACS nano*, vol. 4, no. 7, pp. 3979–3986, 2010.

[25] C. Chen, W. Cai, M. Long et al., "Synthesis of visible-light responsive graphene oxide/TiO2 composites with p/n heterojunction," *ACS nano*, vol. 4, no. 11, pp. 6425–6432, 2010.

[26] X. Peng, F. Gao, J. Zhao, J. Li, J. Qu, and H. Fan, "Self-assembly of a graphene oxide/MnFe2O4motor by coupling shear force with capillarity for removal of toxic heavy metals," *Journal of Materials Chemistry A*, vol. 6, no. 42, pp. 20861–20868, 2018.

[27] L. P. Lingamdinne, J. R. Koduru, Y. L. Choi, Y. Y. Chang, and J. K. Yang, "Studies on removal of Pb(II) and Cr(III) using graphene oxide based inverse spinel nickel ferrite nano-composite as sorbent," *Hydrometallurgy*, vol. 165, pp. 64–72, 2016.

[28] X. Xu, Y. Li, G. Zhang, F. Yang, and P. He, "NiO-$NiFe_2O_4$-rGO magnetic nanomaterials for activated peroxymonosulfate degradation of Rhodamine B," *Water*, vol. 11, no. 2, p. 384, 2019.

[29] H. Wang, Q. Yao, C. Wang et al., "A simple, one-step hydrothermal approach to durable and robust superparamagnetic, superhydrophobic and electromagnetic wave-absorbing wood," *Scientific reports*, vol. 6, no. 1, 2016.

[30] L. P. Lingamdinne, Y. L. Choi, I. S. Kim, J. K. Yang, J. R. Koduru, and Y. Y. Chang, "Preparation and characterization of porous reduced graphene oxide based inverse spinel nickel ferrite nanocomposite for adsorption removal of radionuclides," *Journal of hazardous materials*, vol. 326, pp. 145–156, 2017.

[31] L. G. Bach, T. van Tran, T. D. Nguyen, T. van Pham, and S. T. Do, "Enhanced adsorption of methylene blue onto graphene oxide-doped XFe_2O_4 (X= Co, Mn, Ni) nanocomposites: kinetic, isothermal, thermodynamic and recyclability studies," *Research on Chemical Intermediates*, vol. 44, no. 3, pp. 1661–1687, 2018.

[32] W. Yin, S. Hao, and H. Cao, "Solvothermal synthesis of magnetic $CoFe_2O_4$/rGO nanocomposites for highly efficient dye removal in wastewater," *RSC advances*, vol. 7, no. 7, pp. 4062–4069, 2017.

[33] K. Nejati and R. Zabihi, "Preparation and magnetic properties of nano size nickel ferrite particles using hydrothermal method," *Chemistry Central Journal*, vol. 6, no. 1, 2012.

[34] P. T. Lan Huong, N. Tu, H. Lan et al., "Functional manganese ferrite/graphene oxide nanocomposites: effects of graphene oxide on the adsorption mechanisms of organic MB dye and inorganic As (v) ions from aqueous solution," *RSC advances*, vol. 8, no. 22, pp. 12376–12389, 2018.

[35] A. M. K. Pandian, C. Karthikeyan, and M. Rajasimman, "Isotherm and kinetic studies on adsorption of malachite green using chemically synthesized silver nanoparticles," *Nanotechnology for Environmental Engineering*, vol. 2, no. 1, 2017.

[36] M. G. Pillai, I. Regupathi, M. H. Kalavathy, T. Murugesan, and L. R. Miranda, "Optimization and analysis of nickel adsorption on microwave irradiated rice husk using response surface methodology (RSM)," *Journal of Chemical Technology & Biotechnology*, vol. 84, no. 2, pp. 291–301, 2009.

[37] R. K. Upadhyay, N. Soin, and S. S. Roy, "Role of graphene/metal oxide composites as photocatalysts, adsorbents and disinfectants in water treatment: a review," *RSC Advances*, vol. 4, no. 8, pp. 3823–3851, 2014.

[38] S. Kumar, R. R. Nair, P. B. Pillai, S. N. Gupta, M. A. R. Iyengar, and A. K. Sood, "Graphene oxide–MnFe2O4 magnetic nanohybrids for efficient removal of lead and arsenic from water," *ACS Applied Materials & Interfaces*, vol. 6, no. 20, pp. 17426–17436, 2014.

[39] U. Condomitti, A. T. Silveira, G. W. Condomitti, S. H. Toma, K. Araki, and H. E. Toma, "Silver recovery using electrochemically active magnetite coated carbon particles," *Hydrometallurgy*, vol. 147-148, pp. 241–245, 2014.

[40] N. Neethu and T. Choudhury, "Treatment of methylene blue and methyl Orange Dyes in wastewater by grafted titania pillared clay membranes," *Recent patents on nanotechnology*, vol. 12, no. 3, pp. 200–207, 2018.

[41] U. A. Edet and A. O. Ifelebuegu, "Kinetics, isotherms, and thermodynamic modeling of the adsorption of phosphates from model wastewater using recycled brick waste," *Processes*, vol. 8, no. 6, p. 665, 2020.

[42] C. Wu, X. Lou, A. Huang, M. Zhang, and L. Ma, "Thermodynamics and kinetics of pretilachlor adsorption: implication to controlled release from organobentonites," *Applied Clay Science*, vol. 190, article 105566, 2020.